Tuning topological phase transitions in hexagonal photonic lattices made of triangular rods

Hsun-Chi Chan[1] and Guang-Yu Guo[1,2,*]

[1]*Department of Physics and Center for Theoretical Physics, National Taiwan University, Taipei 10617, Taiwan*
[2]*Physics Division, National Center for Theoretical Sciences, Hsinchu 30013, Taiwan*

In this paper we study topological phases in a two-dimensional photonic crystal with broken time ($\mathcal{T}$) and parity ($\mathcal{P}$) symmetries by performing calculations of band structures, Berry curvatures, Chern numbers, edge states, and also numerical simulations of light propagation in the edge modes. Specifically, we consider a hexagonal lattice consisting of triangular gyromagnetic rods. Here the gyromagnetic material breaks $\mathcal{T}$ symmetry while the triangular rods break $\mathcal{P}$ symmetry. Interestingly, we find that the crystal could host quantum anomalous Hall (QAH) phases with different gap Chern numbers (C_g) including $|C_g| > 1$ as well as quantum valley Hall (QVH) phases with contrasting valley Chern numbers (C_v), depending on the orientation of the triangular rods. Furthermore, phase transitions among these topological phases, such as from QAH to QVH and vice versa, can be engineered by a simple rotation of the rods. Our band theoretical analyses reveal that the Dirac nodes at the K and K' valleys in the momentum space are produced and protected by the mirror symmetry (m_y) instead of the $\mathcal{P}$ symmetry, and they become gapped when either $\mathcal{T}$ or m_y symmetry is broken, resulting in a QAH or QVH phase, respectively. Moreover, a high Chern number ($C_g = -2$) QAH phase is generated by gapping triply degenerate nodal points rather than pairs of Dirac points by breaking $\mathcal{T}$ symmetry. Our proposed photonic crystal thus provides a platform for investigating intriguing topological phenomena which may be challenging to realize in electronic systems, and also has promising potentials for device applications in photonics such as reflection-free one-way waveguides and topological photonic circuits.

I. INTRODUCTION

In recent years, electronic and photonic topological insulators [1,2] have attracted enormous attention because these systems exhibit fascinating wave transport properties. In particular, the gapless edge states on the surface or at the interface between these topological insulators are unidirectional and robust against scattering from disorder due to topologically nontrivial properties of their bulk band structures. The electronic quantum anomalous Hall (QAH) phase, first proposed by Haldane [3], is a two-dimensional (2D) bulk ferrromagnetic insulator (Chern insulator) with a nonzero topological invariant called Chern number in the presence of spin-orbit coupling (SOC) but in the absence of applied magnetic fields [4]. Its associated chiral edge states carry dissipationless unidirectional electric current. Excitingly, this remarkable QAH phase was recently observed in ferromagnetic topological insulator films [5]. Moreover, Haldane and Raghu recently proposed the optical analogs of this intriguing QAH phase in photonic crystals made of time-reversal ($\mathcal{T}$) symmetry broken materials [6,7]. This photonic QAH phase has gapless edge states within each topologically nontrivial bulk band gap, and the number of the edge states is determined by the gap Chern number [7]. Such topologically protected edge states are immune to backscattering and are therefore robust against disorder [8,9]. Subsequently, the photonic topological phases in a number of gyromagnetic photonic crystals with broken $\mathcal{T}$ symmetry were proposed [8,10–12] and observed [9,13].

When designing a photonic Chern insulator, one usually starts with a lattice with both $\mathcal{T}$ symmetry and inversion ($\mathcal{P}$) symmetry where doubly degenerate Dirac points may exist at some high symmetry points [7]. In particular, in a 2D lattice with both $\mathcal{P}$ and $\mathcal{T}$ symmetries, the stability of the Dirac points is guaranteed by the Wigner–von Neumann theorem. Furthermore, one can find the double degeneracies by varying just one or two system parameters. When $\mathcal{T}$ symmetry is broken, the Dirac points become gapped, resulting in a QAH phase. Nevertheless, the topological phases in broken $\mathcal{P}$ symmetry Chern insulators have received much less attention, where different mechanisms would be needed [14,15].

Furthermore, the majority of the predicted or realized photonic Chern insulators so far have been limited to the Chern number $|C| = 1$ [8], although in principle the Chern number can be any integer values. Consequently, having systems with $|C| > 1$ is of fundamental interest in studying topological phases. Systems with higher Chern numbers also have practical values. For example, they are useful for designing novel topological devices such as one-way photonic circuits [11,12]. Indeed, it has been recently proposed [10] and demonstrated [13] that photonic Chern insulators of large Chern numbers can be realized in 2D square and hexagonal lattices made of cylindrical rods by tuning the radius of the rods. It would be interesting to find other ways to realize photonic Chern insulators with $|C| > 1$.

Interestingly, recent progress in understanding the novel properties of electronic 2D materials such as graphene and MoS_2 monolayer has led to the discovery of a $\mathcal{T}$ invariant topological phase called quantum valley Hall (QVH) state
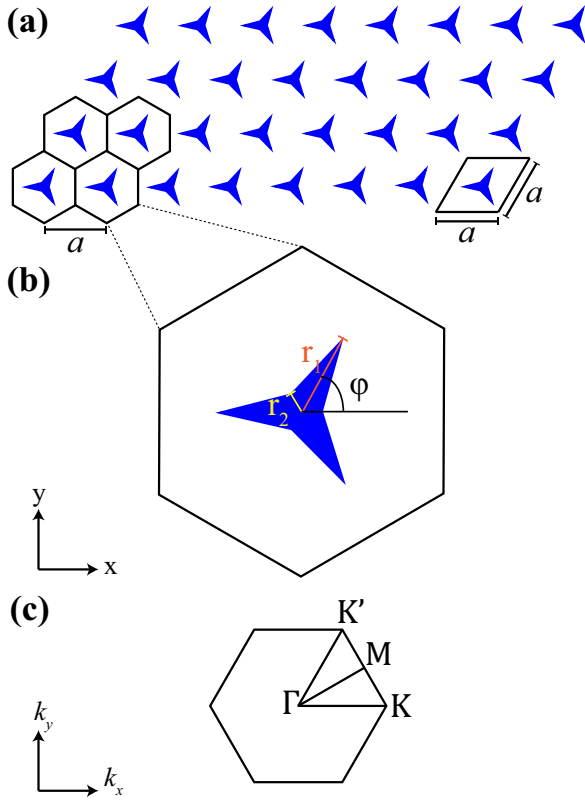
*gyguo@phys.ntu.edu.tw

FIG. 1. (a) Schematic diagram of the hexagonal lattice of triangular gyromagnetic rods in air considered in the present paper. Here a is the lattice constant. (b) Enlarged unit cell containing one triangular rod of $\epsilon = 13$, $\mu = 1$, $\kappa = 0.4$, $r_1 = 0.3075a$, and $r_2 = 0.0615a$. The first Brillouin zone of the hexagonal lattice with high symmetry points labeled.

in broken $\mathcal{P}$ symmetry materials [16–18]. In these QVH materials, the energy extrema (or valleys) of the band structure at the K and K' points in their hexagonal Brillouin zone have contrasting properties such as nonzero Berry curvatures of opposite signs due to the absence of $\mathcal{P}$ symmetry but presence of $\mathcal{T}$ invariance, although they are energetically degenerate [16–20]. This broken valley symmetry results in a number of interesting valley-contrasting phenomena and also a totally new concept of electronics known as valleytronics [17]. Recently, this QVH effect has also been realized in all-dielectric photonic crystals [19,20] and bianisotropic metamaterials [21], and the valley-protected reflection-free propagation of light in the edge modes of these materials has been demonstrated. This would lead to the fascinating prospect of optical communication devices based on the robust flow of light.

In this paper we explore possible topological phases in a 2D photonic crystal with broken $\mathcal{T}$ and $\mathcal{P}$ symmetries. We consider a hexagonal lattice made of triangular gyromagnetic rods, as illustrated in Fig. 1(a). Here the gyromagnetic material breaks $\mathcal{T}$ symmetry while the triangular rods break $\mathcal{P}$ symmetry. Interestingly, we find that the crystal hosts QAH phases with different gap Chern numbers including $|C| > 1$ and QVH phases with contrasting valley Chern numbers, depending on the orientation [i.e., the rotation angle φ in Fig. 1(b)] of the triangular rods. Furthermore, phase transitions among these

topological phases, such as from QAH to QVH and vice versa, can be engineered by a simple rotation of angle φ. Our band theoretical analyses reveal that the Dirac points at the K and K' valleys are produced and protected by the mirror symmetry (m_y) instead of the $\mathcal{P}$ symmetry, and they become topologically gapped when either $\mathcal{T}$ or m_y symmetry is broken, resulting in a QAH or QVH phase, respectively. Moreover, the high Chern number ($C_g = -2$) QAH phase results from gapping triply degenerate nodal points rather than pairs of Dirac points [10] by breaking $\mathcal{T}$ symmetry. Thus, our proposed photonic crystal offers a platform for investigating a number of topological phenomena which may be challenging to realize in electronic systems, and also has promising device applications in photonics.

The rest of this paper is organized as follows. First, we introduce the proposed structure and also describe the computational methods in the next section. Then the main results are presented in Sec. III, including the rich topological gap map on the frequency-rod angle plane in Sec. III A, the representative bulk band structures in Sec. III B, the calculated Berry curvatures in Sec. III C, the gapless edge states in Sec. III D, and reflection immune one-way waveguides in Sec. III E as well as valley Hall edge states and light propagation in Z-shape bends in Sec. III F. Finally, the conclusions drawn from this work are given in Sec. IV.

II. STRUCTURE AND COMPUTATIONAL METHOD

Here we consider a 2D photonic crystal consisting of triangular gyromagnetic rods arranged in a hexagonal lattice filled with air, as shown in Fig. 1(a). The $\mathcal{T}$ symmetry is broken by the gyromagnetic rods used. The permeability tensor of the gyromagnetic material in SI units can be expressed as

$$\boldsymbol{\mu} = \mu_0 \begin{pmatrix} \mu_r & i\kappa & 0 \\ -i\kappa & \mu_r & 0 \\ 0 & 0 & 1 \end{pmatrix}. \quad (1)$$

Following Ref. [8] we neglect the small loss and dispersion, and thus set the material parameters $\epsilon_r = 13$, $\mu_r = 1$, and $\kappa = 0.4$. Note that these parameter values are close to such real gyromagnetic materials as yttrium-iron-garnet [9,13], which has $\mu_r = 0.9$ and $\kappa = 0.4$ at 13 GHz with 0.1 T static magnetic field [22].

The triangular rods are determined by two geometric parameters r_1 and r_2, as indicated in Fig. 1(b). In our numerical simulations, we set $r_1 = 0.3075a$ and $r_2 = 0.0615a$ where a is the lattice constant. Nevertheless, our conclusions will not be affected by this particular choice of the parameters. The structure will be completely fixed only when the angle (φ) between one of the arms and the x axis is specified [see Fig. 1(b)], and this angle is the principal parameter that one tunes to manipulate the properties of the structure, as will be presented in the next section. The structure has the C_{3v} symmetry with three threefold C_3 rotations and three mirror (m_v) reflections, for $\varphi = n \times 30°$ and $n = 0,1,2,3,4,5$. The mirror symmetries contain m_y (reflection plane normal to $\hat{y}$) if $n = 0,2,4$ but include m_x (reflection plane normal to $\hat{x}$) if $n = 1,3,5$. The Brillouin zone (BZ) is also hexagonal, as shown in Fig. 1(c). However, the irreducible BZ wedge (IBZW) depends on angle φ. For example, when $\varphi = 0°$, the IBZW
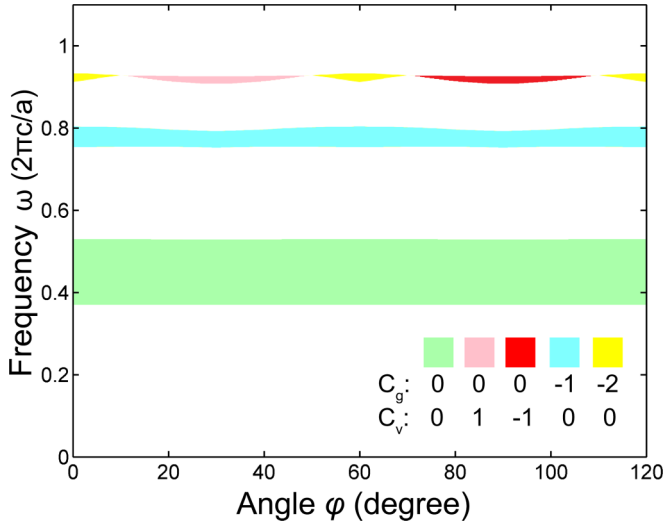
FIG. 2. Topological band gap map on the plane of rotation angle φ and frequency ω. Rotation angle φ is defined in Fig. 1(b). Each band gap region is labeled with a color representing its gap Chern number C_g and valley Chern number C_v. Note that in the third band gap region, as φ increases, a series of topological phase transitions occur from $C_g = -2 (C_v = 0)$ to $C_g = 0 (C_v = 1)$ at $\varphi = \sim10°$, back to $C_g = -2 (C_v = 0)$ at $\varphi = \sim50°$, then to $C_g = 0 (C_v = -1)$ at $\varphi = \sim70°$, and finally back to $C_g = -2 (C_v = 0)$ at $\varphi = \sim110°$.

is $\Gamma K M \Gamma$ since K and K' are equivalent. In contrast, when $\varphi = 30°$, the IBZW is $\Gamma K M K' \Gamma$ because K and K' are no longer equivalent [see Fig. 1(c)].

To calculate the band structure of the proposed structure, we solve the Maxwell's wave equation

$$\nabla \times [\mu^{-1}(\mathbf{r})\nabla \times \mathbf{E}(\mathbf{r})] = \epsilon(\mathbf{r})\omega^2\mathbf{E}, \quad (2)$$

where $\mu(\mathbf{r})$ and $\epsilon(\mathbf{r})$ are the permeability and permittivity tensors, respectively, and ω is the eigenfrequency. We use the finite-element method implemented in the commercial software COMSOL Multiphysics ® [23]. To examine the topological nature of a band gap in the band structure, we also calculate the band Chern number

$$C_n = \frac{1}{2\pi} \int_{\text{BZ}} \Omega_n(\mathbf{k}) \cdot d^2\mathbf{k}, \quad (3)$$

where the integral is over the BZ and $\Omega_n(\mathbf{k})$ is the Berry curvature of the nth band defined as [16]

$$\Omega_n(\mathbf{k}) = \nabla_{\mathbf{k}} \times \mathcal{A}_n(\mathbf{k}), \quad (4)$$

where $\mathcal{A}_n(\mathbf{k}) = \langle E_{n\mathbf{k}}|i\nabla_{\mathbf{k}}|E_{n\mathbf{k}}\rangle$ is the Berry connection and $E_{n\mathbf{k}}$ is the nth band energy. Here we adopt the efficient numerical algorithm reported in Ref. [24] to calculate the band Chern numbers. Note that the Berry curvature Ω_n and the Chern number C_n are invariant under gauge transformation, while $\mathcal{A}_n$ is gauge dependent. Consequently, one advantage of the algorithm is that we can obtain C_n via Eq. (3) without any gauge-fixing process. Thanks to the efficiency of the algorithm [24], we can obtain the accurate C_n even using a moderate dense k-point mesh, and this enables us to perform massive calculations for searching candidate structures or plotting topological gap map such as Fig. 2 [13].

The integer Chern number C_n is the topological invariant of the nth energy band. The sum of the Chern numbers of all the bands below a band gap is called the gap Chern number C_g [10,25]. According to the bulk-edge correspondence [25], the number of gapless edge states between two topologically distinct materials equals the gap Chern number difference across the interface.

III. RESULTS AND DISCUSSION

A. Topological gap map

To have an overall picture of the topological phases and phase transitions in the proposed triangular photonic crystal, we construct a topological gap map in the plane of rotation angle φ and frequency ω, as displayed in Fig. 2. Since we find that the period of the rotation angle is 120°, we calculate the band gaps as a function of the rotation angle from $\varphi = 0°$ to $\varphi = 120°$ with the angle step $\Delta\varphi = 1°$.

Figure 2 shows that there are three band gap regions in the frequency range from 0 to 1 $2\pi c/a$. The topological nature of a band gap in a broken $\mathcal{T}$ symmetry system can be characterized by the gap Chern number (C_g), which is the sum of the Chern numbers of all the bands below the band gap, as mentioned above in Sec. II. Therefore, the first band gap near 0.5 $2\pi c/a$ is topologically trivial because its gap Chern number $C_g = 0$. The second band gap just below 0.8 $2\pi c/a$ is topologically nontrivial and its gap Chern number $C_g = -1$. Moreover, the band gap is rather large, being around 7% (0.056 $2\pi c/a$). Interestingly, when rotational angle φ varies from 0° to 120°, the third band gap experiences a series of topology changes (see Fig. 2). For example, as φ increases, the topological phase changes from $C_g = -2 (C_v = 0)$ to $C_g = 0 (C_v = 1)$ at $\varphi = \sim10°$, and from $C_g = -2 (C_v = 0)$ to $C_g = 0 (C_v = -1)$ at $\varphi = \sim70°$. Here C_v is the valley Chern number [16] of the gap (see Sec. III D below). The gap and valley Chern numbers in the vicinity of $\varphi = 0°, 60°, 120°$ are $C_g = -2$ and $C_v = 0$, while they are $C_g = 0$ and $C_v = 1 (C_v = -1)$ in the region centered at $\varphi = 30° (\varphi = 90°)$. Figure 2 thus shows that the angle period is 120° rather than 60°. Although the system has the same Chern number of 0 for $\varphi = 30°$ and $\varphi = 90°$, its valley Chern numbers at these φ values have opposite signs. Clearly, such a topological gap map provides us useful information for, e.g., designing photonic topological insulators and hence reflection-free one-way waveguides as well as for engineering topological phase transitions. Characteristics of the band gaps for the $\varphi = 0°$ and $\varphi = 30°$ cases are listed in Table I.

B. Bulk band structures

To understand the formation mechanisms of the topological gaps and also other interesting properties of the triangular photonic crystal, we present the calculated band structures for the $\varphi = 0°$ and $\varphi = 30°$ cases in Figs. 3(a) and 3(b), respectively. The TM mode (i.e., $\mathbf{E} = E_z\hat{z}$) is considered here. To see how the band structure evolves when dielectric triangular rods are replaced by gyromagnetic rods, both band structures of $\kappa = 0.4$ and $\kappa = 0$ are presented. Adding a nonzero off-diagonal element (κ) to the permeability tensor [Eq. (1)] breaks $\mathcal{T}$ symmetry.

TABLE I. Calculated band gap ($\Delta\omega_g$), relative band gap ($\Delta\omega_g/\omega_m$), gap Chern number (C_g), valley Chern number (C_v), and number of one-way edge states (N_g) for the $\varphi = 0°$ and $\varphi = 30°$ cases. Here $\Delta\omega_g = \omega_2 - \omega_1$, gap center $\omega_m = (\omega_1 + \omega_2)/2$, where ω_1 (ω_2) is the highest (lowest) frequency of the lower (upper) band of the gap. As a measure of unidirectionality, the edge state intensity ratio (I_-/I_+) of wave propagation along the interface between the crystal and the metal wall (see Sec. III E) is also listed. Here I_- and I_+ are the averaged intensities at $x = -20a$ and $x = 6a$, respectively.

Structure	$\varphi = 0°$			$\varphi = 30°$		
Gap number	1st	2nd	3rd	1st	2nd	3rd
$\Delta\omega_g$ ($2\pi c/a$)	0.16	0.056	0.021	0.16	0.041	0.018
$\Delta\omega_g/\omega_m$ (%)	36	7.3	2.3	35	5.2	2.0
C_g	0	-1	-2	0	-1	0
C_v	0	0	0	0	0	1
N_g	0	1	2	0	1	0
I_-/I_+ (10^3)	–	1400	6	–	23	–

Several observations can be drawn from an examination of Fig. 3. First, when $\kappa = 0$ and hence the system has the $\mathcal{T}$ symmetry, the energy bands (red dotted lines) along the $\Gamma K M \Gamma$ and $\Gamma K' M \Gamma$ lines are identical [see Figs. 3(a) and 3(b)]. This is because the $\mathcal{T}$ symmetry ensures $\omega(-\mathbf{k}) = \omega(\mathbf{k})$ [26]. Second, when $\varphi = 0°$ and $\kappa = 0$, there are doubly degenerate points (i.e., the Dirac points) at the K and K' points [see red dotted lines near $\omega = 0.6\ 2\pi c/a$ in Fig. 3(a)]. In contrast, the $\varphi = 30°$ case has no such degenerate points [see red dotted lines in Fig. 3(b)]. This results from the fact that the $\varphi = 0°$ geometry has three mirror m_y reflections (i.e., three vertical reflection planes along KK' direction) while the $\varphi = 30°$ structure lacks such mirror m_y symmetry. In other words, the Dirac points at K and K' points in the $\varphi = 0°$ structure occur because of the presence of both $\mathcal{T}$ and m_y symmetries. Third, Fig. 3 shows that when $\kappa = 0$, there are doubly degenerate points (i.e., massive Dirac nodes) (see red dotted lines close to $\omega = 0.75\ 2\pi c/a$) at the center of the

BZ (the Γ point). When the κ becomes nonzero and hence $\mathcal{T}$ symmetry is broken, the double degeneracies are lifted and the Dirac nodes become gapped. When these Dirac nodes become gapped due to broken $\mathcal{T}$ symmetry, the two bands would exchange 2π Berry phase (see Fig. 4), giving rise to a nontrivial gap. Finally, Fig. 3(a) shows that there are triply degenerate nodal points at the K and K' points near $\omega = 0.92\ 2\pi c/a$. These rare triply degenerate nodal points are caused by the accidental degeneracy of a doubly degenerate Dirac point and a nondegenerate band. Fascinatingly, it was shown that photonic crystals with a triply degenerate nodal point at the Γ point may be used to realize zero-refractive-index metamaterials [27]. These interesting threefold nodal points were recently found in topological phonic crystals [28]. More recently, they were also predicted in several electronic topological metals [29,30] and subsequently observed in topological semimetal MoP [31]. All these indicate that the triply degenerate nodal points are attracting increasing attention in the field of electronic, phononic, and photonic topological materials.

The topological nature of a band gap in a broken $\mathcal{T}$-symmetry structure can be characterized by the gap Chern number (C_g), as mentioned before in Sec. II. The calculated band Chern numbers displayed in Fig. 3 indicate that the first band gap with $C_g = 0$ is topologically trivial in both $\varphi = 0°$ and $\varphi = 30°$ cases. In contrast, the second band gap is a QAH phase with $C_g = -1$ [see Figs. 3(a) and 3(b)]. Note that this band gap results from the lifting of the doubly degenerate Dirac nodes at the Γ point by breaking the $\mathcal{T}$ symmetry, which exist in both $\varphi = 0°$ and $\varphi = 30°$ cases. Remarkably, in the $\varphi = 0°$ case the third band gap is a high Chern number QAH phase with $C_g = -2$ [Fig. 3(a)]. This interesting band gap results from gapping the rare triply degenerate nodal points at the K and K' points by broken $\mathcal{T}$ symmetry ($\kappa = 0.4$). Thus, the gap Chern number ($|C_g|$) is larger than 1. Interestingly, this large Chern number gap would allow us to create multimode one-way edge states and hence waveguides [10]. In the $\varphi = 30°$ case, on the other hand, the band gap is a QVH phase with valley Chern number $C_v = 1$ [Fig. 3(b)], which will be discussed

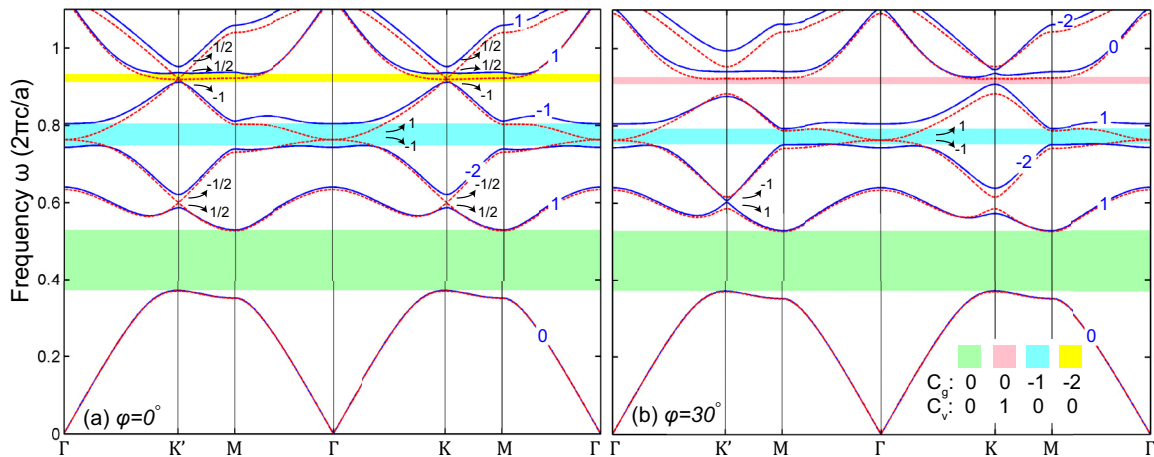FIG. 3. Band structures of the photonic crystal with (a) $\varphi = 0°$ and (b) $\varphi = 30°$. Both $\mathcal{T}$-invariant ($\kappa = 0$, red dotted lines) and $\mathcal{T}$-symmetry broken ($\kappa = 0.4$, blue solid lines) band structures are displayed. In the $\kappa = 0.4$ case, the band Chern numbers are labeled by integers. The black arrows and numbers illustrate how Chern number exchange between two adjacent bands. Note that the second band gap (blue region) is a QAH phase with the gap Chern number $C_g = -1$. Interestingly, the third band gap in (a) is a QAH phase with $C_g = -2$ (yellow region), while in (b) is a QVH phase with the valley Chern number $C_v = 1$ (pink region).
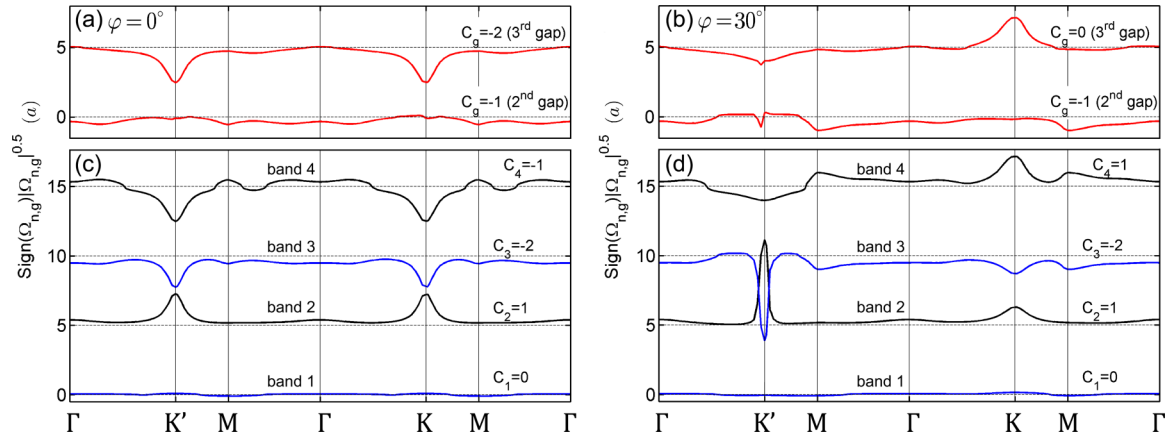
FIG. 4. Gap Berry curvatures Ω_g [(a) and (b)] and band Berry curvatures Ω_n [(c) and (d)], respectively, for the photonic crystal with $\varphi = 0°$ [(a) and (c)] and $\varphi = 30°$ [(b) and (d)]. For clarity, $\text{sgn}(\Omega_g)|\Omega_g|^{1/2}$ for the third gap in (a) and (b) has been shifted upwards by $5a$, and $\text{sgn}(\Omega_n)|\Omega_n|^{1/2}$ in (c) and (d) has been shifted upwards by $5a$, $10a$, and $15a$ for bands $n = 2, 3$, and 4, respectively. The black dotted lines indicate the zero value positions.

in the next subsection. Note that the third gap already occurs when $\kappa = 0$ and thus is not caused by broken $\mathcal{T}$ symmetry [Fig. 3(b)]. Instead, it results from broken m_y mirror symmetry. Nonetheless, when κ becomes nonzero (e.g., $\kappa = 0.4$), this gap at the K point becomes larger. Interestingly, in contrast, this gap at the K' point becomes smaller when κ becomes nonzero.

Lastly, Fig. 3 shows that when κ becomes nonzero, there is no direct overlap between bands 2 and 3 in the entire BZ. Note that there is a small gap between bands 2 and 3 at K' in Fig. 3(b). In other words, there is a continuous gap separating bands 2 and 3 throughout the BZ and hence bands 2 and 3 have a well-defined band Chern number. Furthermore, this gap is topologically nontrivial since it has a nonzero gap Chern number of $+1$. Nonetheless, this gap is not marked on the gap map in Fig. 2 simply because it is not a complete gap due to the indirect overlap between bands 2 and 3.

C. Berry curvatures

In order to unravel how the C_n numbers exchange between neighboring bands as well as the resultant C_g arises, we calculate the band Berry curvatures $\Omega_n(\mathbf{k})$ for all the four bands below the third band gap (see Fig. 3) and plot these Berry curvatures for $\varphi = 0°$ and $\varphi = 30°$ in Fig. 4. Note that in Fig. 4 we plot $\text{sgn}(\Omega_{n,g})|\Omega_{n,g}|^{1/2}$ in order to better reveal the variation of the Berry curvature with $\mathbf{k}$. Here we follow Ref. [32] where the band-decomposed spin Berry curvatures helped to reveal the origin of the gigantic spin Hall conductivity in platinum metal. It turns out that gapping the degenerate points at K and Γ cause quite different Berry curvatures. We also evaluate the gap Berry curvatures $\Omega_g(\mathbf{k})$ given by

$$\Omega_g(\mathbf{k}) = \sum_n \Omega_n(\mathbf{k}), \qquad (5)$$

where the summation is over all the band Berry curvature $\Omega_n(\mathbf{k})$ below the gap. An integration of $\Omega_g(\mathbf{k})$ over the BZ gives rise to the gap Chern number C_g [10]. The calculated $\Omega_g(\mathbf{k})$ for the second and third gaps for $\varphi = 0°$ and $\varphi = 30°$ are displayed as a function of $\mathbf{k}$ in Fig. 4. The contour plots of $\Omega_g(\mathbf{k})$ on

the $k_z = 0$ plane for the third gap for $\varphi = 0°$ and $\varphi = 30°$ are given in Fig. 5.

Figure 4(a) shows that for bands 2–4, all the band Berry curvatures Ω_n peak at K and K'. Furthermore, the signs of the peaks for bands 2 and 3 are opposite. As mentioned before, with the $\mathcal{T}$ symmetry, the second and third bands touch at K and K' and thus form the massless Dirac points [Fig. 3(a)]. However, when the $\mathcal{T}$ symmetry is broken, these Dirac points become gapped and the second and third bands exchange $\pm 2\pi$ Berry phase [Berry phase $\phi_n = 2\pi C_n$ given by Eq. (3)] and hence $C_n = \pm 1$. This gives rise to the peaks with opposite signs in Ω_n at these Dirac points. Interestingly, if both bands are below the gap of interest, their contributions to the gap Chern number cancel each other and thus become diminished. Therefore, in the present case, the main contribution to the gap Berry curvature and hence the gap Chern number of the third gap comes mainly from the fourth band which has the pronounced peaks at K and K' [Fig. 4(a)]. Interestingly, in the case of $\varphi = 30°$, bands 2 and 3 have a large peak at K' but a small peak at K. Nevertheless, these two peaks with opposite signs cancel each other and hence the dominant contribution to the gap Berry curvature comes predominantly from band 4. However, the band Berry curvatures of band 4 in the regions centered at K and K' have opposite signs [see Figs. 4(b) and 5(b)] and consequently, the gap Chern number of the third gap is zero. In contrast, Fig. 4 shows that the Ω_g of the second gap ($C_g = -1$) varies more smoothly over the BZ, and this could be attributed to the much larger gap opened at the massive Dirac point on the Γ point. Finally, this Ω_g has a small peak at M instead (Fig. 4).

Figures 3 and 4 can also help us to better understand how C_n exchange at the degenerate points when the $\mathcal{T}$ symmetry is broken. For instance, Fig. 4(c) shows that both Ω_2 and Ω_3 have a peak at the K and K', but with opposite signs. This suggests that band 2 and band 3 exchange $\pm 1/2$ Chern number at K' and K, as illustrated by the black arrows at K' and K in Fig. 3(a). Likewise, Ω_3 and Ω_4 have similar behaviors near the Γ. Here the exchanged Chern numbers have opposite signs and this is because gapping the Dirac point at Γ would result in an exchange of ± 1 Chern numbers. Indeed, $C_3 = -1 - 1 = -2$
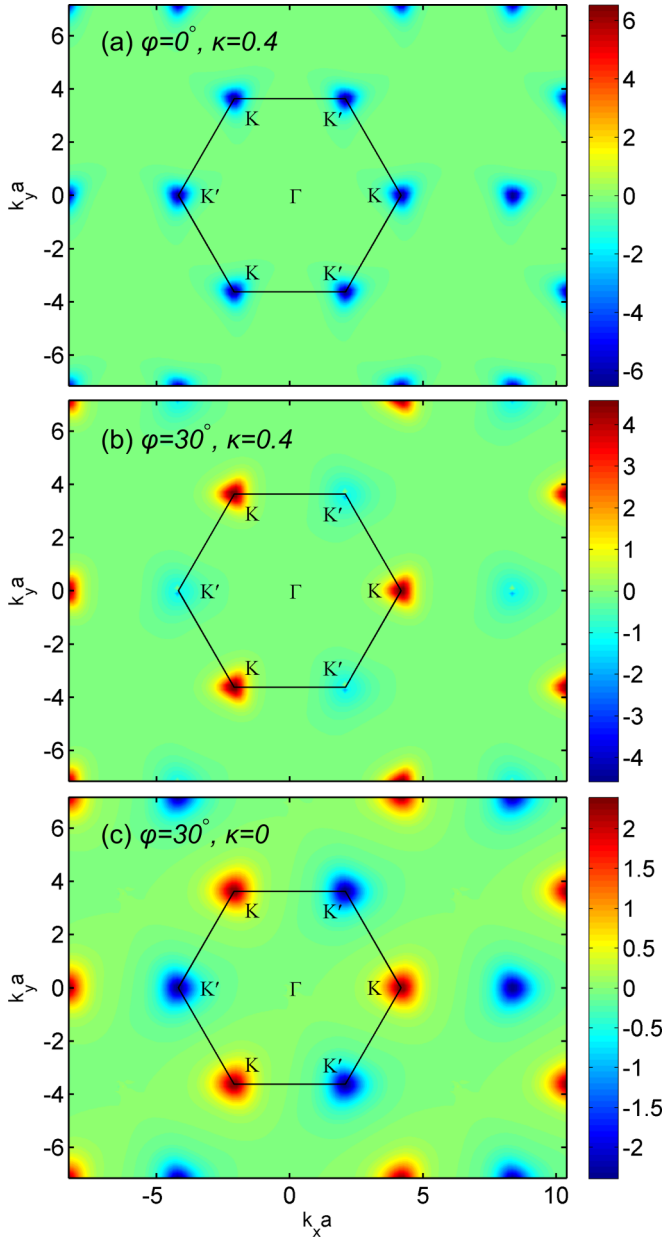
FIG. 5. Contour plots of the third gap Berry curvature $\Omega_g(\mathbf{k})$ of the triangular photonic crystal with (a) $\varphi = 0°$ and $\kappa = 0.4$ ($C_g = -2$), (b) $\varphi = 30°$ and $\kappa = 0.4$ ($C_g = 0$), and (c) $\varphi = 30°$ and $\kappa = 0$ ($C_g = 0$). The values on the color bars are in units of a^2, where a is the lattice constant.

in which band 3 receives -1 from both band 2 and band 4. Interestingly, we find that after gapping the triple degeneracy, the fourth band receives -1 Chern number from the fifth and sixth bands at both K' and K [see Fig. 3(a)] such that $C_4 = 1 - 1 - 1 = -1$ where $+1$ Chern number comes from band 3, being consistent with the negative peaks seen at the K and K' in Fig. 4(a).

Finally, let us examine the calculated gap Berry curvature $\Omega_g(\mathbf{k})$ over the entire 2D BZ. Figure 5(a) shows clearly that in the $\varphi = 0°$ case, the $\Omega_g(\mathbf{k})$ of the third gap has six pronounced negative peaks, respectively, at six K and K'

points, although it is rather flat with a small negative value of $|\Omega_g(\mathbf{k})| < 0.5a^2$ over the rest of the BZ. As mentioned above, these six peaks are caused by the lifting of the triply degenerate nodal points at both K and K' points [see Fig. 3(a)] due to the replacement of the dielectric rods ($\kappa = 0$) by the gyromagnetic rods ($\kappa = 0.4$) which breaks the $\mathcal{T}$ symmetry. These six peaks are identical because the $\Omega_g(\mathbf{k})$ distribution has the C_{6v} symmetry. Therefore, the integration of the $\Omega_g(\mathbf{k})$ gives rise to a nonzero gap Chern number C_g of -2. Thus, the third gap is a high Chern number QAH phase.

Interestingly, Figs. 5(b) and 5(c) reveal that the three negative peaks at the three K points in the $\varphi = 0°$ case become three large positive peaks in the $\varphi = 30°$ case, caused by a simple rotation of angle φ from $0°$ to $30°$. The $\Omega_g(\mathbf{k})$ in the rest of the BZ is almost zero. The $\Omega_g(\mathbf{k})$ distribution now has the C_{3v} symmetry. Consequently, the contribution from the three positive peaks at the three K points to the C_g cancels that from the three negative peaks at the K' points, resulting in $C_g = 0$. Interestingly, this unique $\Omega_g(\mathbf{k})$ pattern is identical to that in the electronic band structure of MoS$_2$ monolayer [18,33], and thus is the signature of the QVH phase with nonzero valley Chern number of $C_v = +1$ [19,20]. Here C_v is defined as the difference between two valley indices C^K and $C^{K'}$, i.e., $C_v = C^K - C^{K'}$ [19,20]. The valley index C^K ($C^{K'}$) can be obtained by integrating the gap Berry curvature $\Omega_g(\mathbf{k})$ over half of the IBZW in the vicinity of the K (K') point. In the $\varphi = 0°$ case, clearly this would give rise to $C^K = +1/2$ and $C^{K'} = -1/2$ [see Fig. 5(c)], thus leading to $C_v = +1$. A further rotation of φ by another $30°$ would make the system return to the case of $\varphi = 0°$, i.e., the cases of $\varphi = 60°$ and $\varphi = 0°$ have the same $\Omega_g(\mathbf{k})$ distribution. [Thus, the $\Omega_g(\mathbf{k})$ of $\varphi = 60°$ is not shown here.] Another rotation of φ by $30°$ to $\varphi = 90°$ would lead to a $\Omega_g(\mathbf{k})$ pattern that is identical to that of the $\varphi = 30°$ case except a swap of K and K' points. [Thus, the $\Omega_g(\mathbf{k})$ of $\varphi = 90°$ is not shown here.] However, the two valley indices would swap signs, thereby resulting in a valley Chern number of $C_v = -1$. This shows that the properties of the system as a function of φ has a period of $120°$.

D. Chiral edge states

The principle of bulk-edge correspondence guarantees that gapless one-way (chiral) edge states occur at the interface between two topologically different bulk insulators and the number of these edge states equals to the difference in the gap Chern numbers of the two insulators (see, e.g., [2]). To further study these fascinating edge states, we calculate the edge band diagram, i.e., frequency dispersions $\omega(\mathbf{k}_\parallel)$ for the wave vector $k_\parallel$ along the edge of the photonic crystal for both $\varphi = 0°$ and $\varphi = 30°$, as displayed in Figs. 6(a) and 6(b), respectively. In this calculation, a supercell consisting of one unit cell along the interfacial x direction [also the propagation direction ($k_\parallel = \hat{x}k_x$)] and 20 unit cells of $\varphi = 0°$ [Fig. 6(a)] and $\varphi = 30°$ [Fig. 6(a)] photonic crystals along KK' direction with both ends terminated by a perfect electric conductor (PEC). Here the PEC is adopted to mimic a metal in the microwave region [8,10].

Figure 6 shows that apart from bulk projected bands (blue curves), there are one gapless edge band (red lines) in the
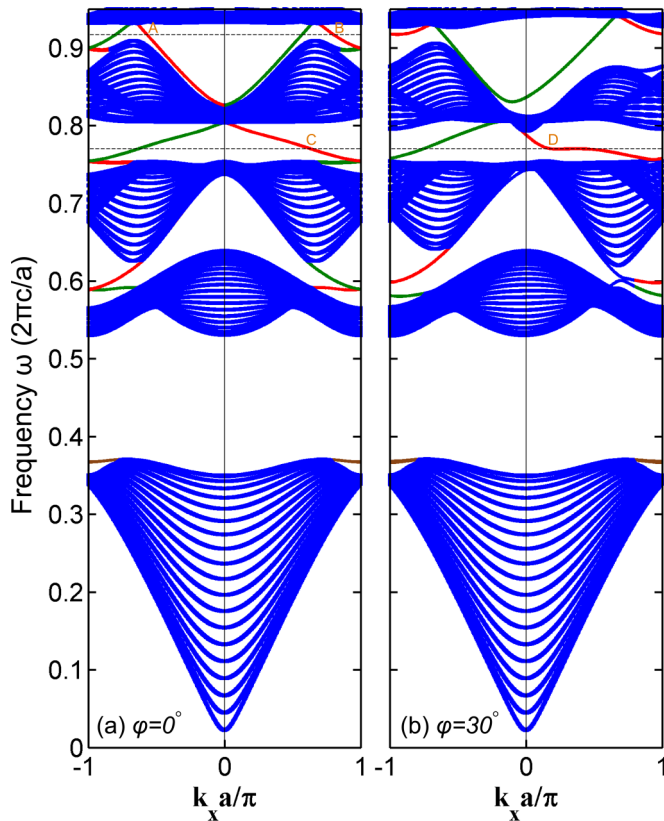
FIG. 6. Edge band diagram of the gyromagnetic photonic crystal ribbon of (a) $\varphi = 0°$ and (b) $\varphi = 30°$ with both edges terminated by a perfect electric conductor. The red (green) lines represent upper (lower) edge bands, while the blue curves denote bulk projected bands. The brown lines at the top of bulk band 1 denote doubly degenerate upper and lower edge bands. The field profiles of the edge states at the cross points of the dotted horizontal lines and edge bands and marked as A, B, C, D, are shown in Fig. 7. The slopes of gapless edge bands (i.e., their group velocities $\partial \omega / \partial k$) indicate the wave propagation directions. One one-way edge band for each edge is observed in the second gap while (a) two and (b) zero one-way edge band at each edge exist in the third gap. These agree well with the calculated C_g shown in Fig. 3.

FIG. 7. Electric field profiles ($|E_z|$) of the edge states labeled A, B, C, and D in Fig. 6. The color bar is in units of V/m. In each panel, the orange line on the top represents the metallic wall at the edge of the metastructure.

E. Reflection immune one-way waveguides

In this subsection we should demonstrate that topologically protected one-way edge modes propagate at the interface of a Chern photonic crystal with another topologically different material by performing numerical simulations of electromagnetic (EM) wave propagations along the interface. We will also access their application potentials such as reflection-free one-way waveguides. Both the second and third topological gaps of the $\varphi = 0°$ photonic crystal [see Fig. 3(a)] will be considered. Let us first study the interface between two topological distinct photonic crystals, namely, $\varphi = 0°$ ($C_g = -2$) and $\varphi = 30°$ ($C_g = 0$), with the source frequency in the third band gap. As illustrated in Fig. 8(a), the simulation system used consists of the $\varphi = 0°$ crystal (lower region) and the $\varphi = 30°$ crystal ($C_g = 0$) (upper region). A point source, which radiates in all directions with frequency $\omega = 0.92 \, 2\pi c/a$ in the third gap, is placed at the origin (green star) in the interface. Moreover, as an obstacle to the EM wave propagation, a metallic plate (orange line) of thickness $0.1a$ and width $4a$ is inserted at $-11a$ with the plate surface tilted $\varphi = 30°$ away from y axis [Fig. 8(a)]. The $\mathrm{Re}(E_z)$ field distribution displayed in Fig. 8(a) demonstrates first that the EM wave cannot enter the upper and lower regions because the operating frequency is in the band gap, and second that it cannot go right (the $\hat{x}$ direction) because it is forbidden by the topological nature of the edge state. For example, the ratio (I_-/I_+) of the light intensity at $-17a$ to that at $6a$ is $\sim 3.8 \times 10^3$. Such a significant difference is the signature of unidirectionality. Therefore, the EM wave effectively can only propagate toward the $-\hat{x}$ direction. Furthermore, as expected, the EM wave can circumvent the metallic plate and continue traveling towards the $-\hat{x}$ without loss [see the calculated intensity as a function of the distance from the source in Fig. 8(b)]. In particular, the ratio of the transmitted intensities at $-17a$ to that at $-7a$ is ~ 0.990, indicating that the scattering due to the obstacle (the metal plate) is minimal.

second gap region, which agree well with calculated $C_g = -1$ shown in Fig. 3. Similarly, in Fig. 6(a) we can see two edge bands in the third gap ($C_g = -2$). Note that the slopes of the edge bands indicate the direction of propagation (i.e., their group velocities $\partial \omega / \partial k$). In Fig. 6 the negative slopes of edge bands suggest that the waves would propagate towards the $-\hat{x}$ direction. On the other hand, as shown in Fig. 6(b), no gapless one-way edge band is observed in the third gap, being consistent with $C_g = 0$ in Fig. 3. All these observations show that bulk-edge correspondence is satisfied. Moreover, the $|(E_z)|$ field profiles of the edge states labeled as A, B, C, and D are shown in Fig. 7. Clearly the electric fields of edge states C and D from the second band gap are more confined to the edge than that of the A and B states in the third gap (Fig. 7), simply because the second band gap is wider (Table I). Finally, we can also see one chiral edge band in the incomplete gap near $0.62 \, \pi c/a$ in Fig. 6, as can be expected from its nonzero gap Chern number of $+1$ shown in Fig. 3.
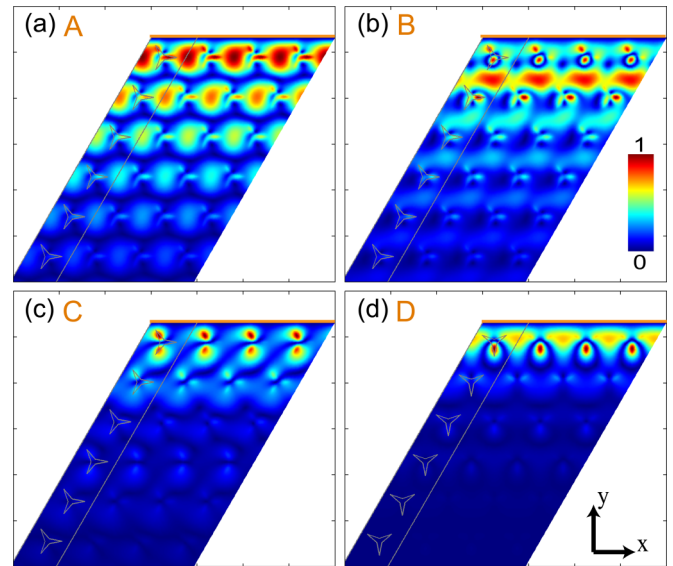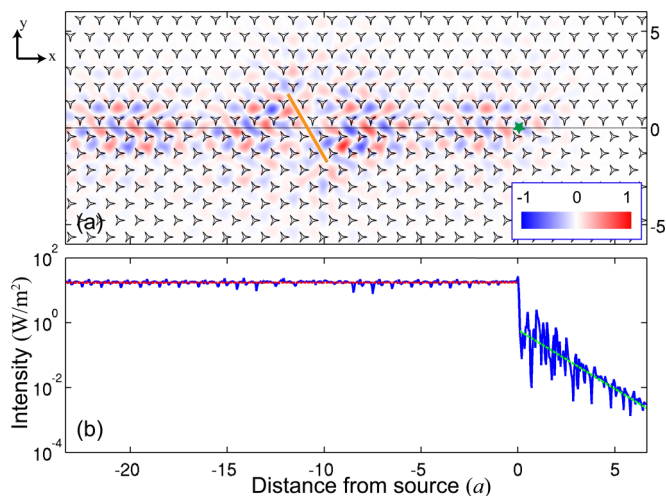
FIG. 8. Numerical simulation of wave propagation in an interfacial state between two topologically distinct photonic crystals of $\varphi = 0°$ ($C_g = -2$) and $\varphi = 30°$ ($C_g = 0$) with a point source of frequency $\omega = 0.92\, 2\pi c/a$ within the third topological gap (see Fig. 3). (a) Calculated Re(E_z) distribution. The values on the color bar are in units of V/m. The upper region is the $\varphi = 30°$ photonic crystal and the lower region is the $\varphi = 0°$ photonic crystal. The green star denotes the point source. The orange line at $-11a$ represents a metallic plate of thickness $0.1a$ and width $4a$ with the plate surface tilted $\varphi = 30°$ away from y axis. (b) Intensity (I) as a function of the distance from the point source. Here I is defined as the integrated intensity over the cross section divided by the area of the cross section.

For the application as a waveguide, the surface of a photonic topological insulator is usually covered with a metal (e.g., copper) wall. Therefore, we also perform similar simulations for the interface between the $\varphi = 0°$ photonic crystal and a metallic wall which is topologically trivial. In principle, the larger the topological gap, the better the localization of the EM wave in the interfacial region. As a result, from the viewpoint of the application of the edge modes as one-way waveguides, it would be advantageous to use a larger band gap. Therefore, we consider the $\varphi = 0°$ photonic crystal with the source frequency being $\omega = 0.92\, 2\pi c/a$ within the third gap ($C_g = -2$, $E_g = 2.3\%$) and also $\omega = 0.78\, 2\pi c/a$ within the second gap ($C_g = -1$, $E_g = 7.3\%$). The calculated Re(E_z) field and also the transmission intensity are displayed in Figs. 9 and 10, respectively. Indeed, Fig. 10(a) shows that the Re(E_z) field is more confined to the interfacial region compared to that shown in Fig. 9. Moreover, the unidirectionality of the edge mode in the second gap is much better than that of the third gap. This is reflected in the fact that the ratio (I_-/I_+) of the wave intensity at $-17a$ to that at $6a$ in Fig. 10 is nearly three orders of magnitude higher than in Fig. 9 (see Table I). Interestingly, Fig. 2 shows that the topological nature of the second gap does not depend on the rotation angle φ. As a result, the reflection-free one-way waveguiding would be very robust against the disorders such as the imperfect alignments of the triangular rods in the photonic crystal introduced during the waveguide fabrication processes.

The main properties of the band gaps such as the gap sizes, the gap Chern numbers (C_g), the numbers of edge states (N_g), and on-and-off edge intensity ratio (I_-/I_+) are listed in Table I.
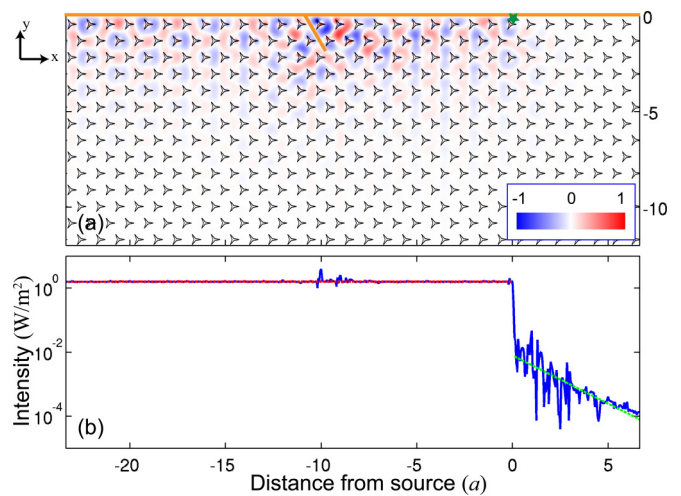

FIG. 9. Numerical simulation of wave propagation in an interfacial state between the photonic crystal of $\varphi = 0°$ ($C_g = -2$) and a metallic wall with a point source of frequency $\omega = 0.92\, 2\pi c/a$ within the third gap [see Fig. 3(a)]. (a) Calculated Re(E_z) distribution. The values on the color bar are in units of V/m. The lower region is the $\varphi = 0°$ photonic crystal and the metallic wall (orange line) is on the top of the photonic crystal. The green star denotes the point source. The orange line at $-11a$ represents a metallic plate of thickness $0.1a$ and width $2a$ with the plate surface tilted $\varphi = 30°$ away from y axis. (b) Intensity (I) as a function of the distance from the point source. Here I is defined as the integrated intensity over the cross section divided by the area of the cross section.

First, Table I shows that the second gap sizes ($C_g = -1$) in both $\varphi = 0°$ and $\varphi = 30°$ cases are large, being comparable to some well-known designs using circular rods [8,10]. Second, that $|C_g| = N_g$ confirms the bulk-edge correspondence, as mentioned before. Lastly, the large magnitudes of I_-/I_+ especially of $\sim 10^6$ for the second gap indicates that the waveguides made of the proposed photonic crystals would have a very high unidirectionality. This unidirectionality also manifests itself as a sharp drop in the intensity at the right-hand side of the point source towards the $+\hat{x}$ direction in Figs. 8–10(b).

F. Valley Hall edge states and light propagation in a Z-shape bend

The above examination of the $\Omega_g(\mathbf{k})$ of the third gap over the BZ in Sec. III C reveals the interesting QVH phase in both $\varphi = 30°$ (valley Chern number $C_v = +1$) and $\varphi = 90°$ (valley Chern number $C_v = -1$) cases. The occurrence of this QVH phase is caused by a rotation of the triangular rods by $30°$ from $\varphi = 0°$ to $\varphi = 30°$. In the $\varphi = 0°$ case where both the $\mathcal{T}$ symmetry and the mirror symmetry m_y exist, there are six Dirac cones of bands 4–6 [Fig. 3(a), red curves] at six K and K' points, respectively. When the system is transformed to the $\varphi = 30°$ case, the mirror symmetry m_y is broken and the Dirac points become gapped [Fig. 3(b), red curves], leading to nonzero Berry curvature with the odd symmetry [16], i.e., $\Omega_g(-\mathbf{k}) = -\Omega_g(\mathbf{k})$ [see also Fig. 5(c)]. An integration of $\Omega_g(\mathbf{k})$ over the BZ is zero, as required by the $\mathcal{T}$ symmetry. As mentioned before, the $\varphi = 90°$ case has the same $\Omega_g(\mathbf{k})$ pattern as that of the $\varphi = 30°$ case except a swap of K and K'
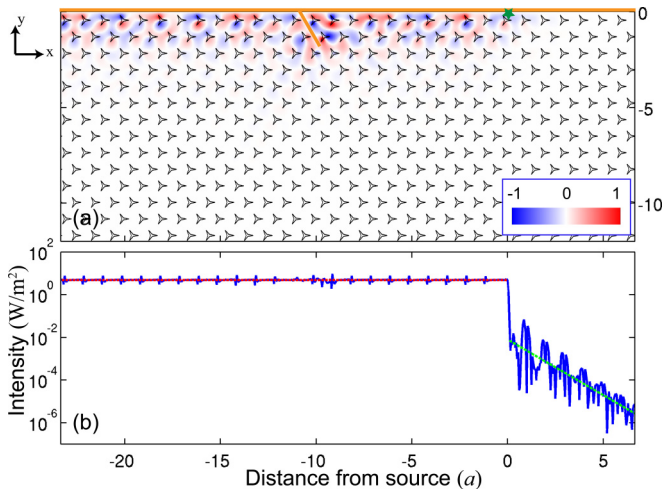
FIG. 10. Numerical simulation of wave propagation in an interfacial state between the photonic crystal of $\varphi = 0°$ ($C_g = -1$) and a metallic wall with a point source of frequency $\omega = 0.78\, 2\pi c/a$ within the second gap [see Fig. 3(a)]. (a) Calculated $\mathrm{Re}(E_z)$ distribution. The values on the color bar are in units of V/m. The lower region is the $\varphi = 0°$ photonic crystal and the metallic wall (orange line) is on the top of the photonic crystal. The green star denotes the point source. The orange line at $-11a$ represents a metallic plate of thickness $0.1a$ and width $2a$ with the plate surface tilted $\varphi = 30°$ away from y axis. (b) Intensity (I) as a function of the distance from the point source. Here I is defined as the integrated intensity over the cross section divided by the area of the cross section.

points, i.e., the third band gap of the $\varphi = 90°$ case is also a QVH phase but with $C_v = -1$.

Surprisingly, when $\mathcal{T}$ symmetry is broken (i.e., $\kappa = 0.4$), the gap Berry phase of the third gap remains zero. The topology of bands 4–6 remains unaltered and this can also be seen by comparing bands 4–6 in the vicinity of the K and K' points in Fig. 3(b) before (red curves) and after (blue curves) the introduction of the gyromagnetic material. Therefore, the third gap in the $\kappa = 0.4$ and $\varphi = 30°$ case is also a QVH phase with $C_v = +1$. Since $\mathcal{T}$ symmetry is now broken, the QVH phase should be called the pseudo-QVH phase, as for the pseudoquantum spin Hall phases [34,35]. Nonetheless, the profiles of the Berry curvatures at K and K' valleys now become different, as shown in Fig. 5(b).

It is known that the edge states in a QVH photonic topological insulator is valley dependent and thus the intervalley scattering along the zigzag boundary [20,36] is suppressed. This would lead to valley-protected robust wave propagation in a Z-shape bend between two QVH photonic crystals with different valley Chern numbers. Therefore, to explicitly verify the QVH phases in the $\varphi = 30°$ and $\varphi = 90°$ crystals, we performed numerical simulations of light propagation along a Z-shape interface between these two topologically distinct crystals, as shown in Fig. 11. Figure 11(a) shows that in the $\kappa = 0.0$ case, the wave can turn around the two sharp corners, thus proving the existence of the QVH edge states at the interface. The same situation also occurs in the $\kappa = 0.4$ case [Fig. 11(b)], thereby suggesting that the QVH edge states also exist in the interface between the $\kappa = 0.4$ photonic crystals. Therefore, the results of these numerical simulations
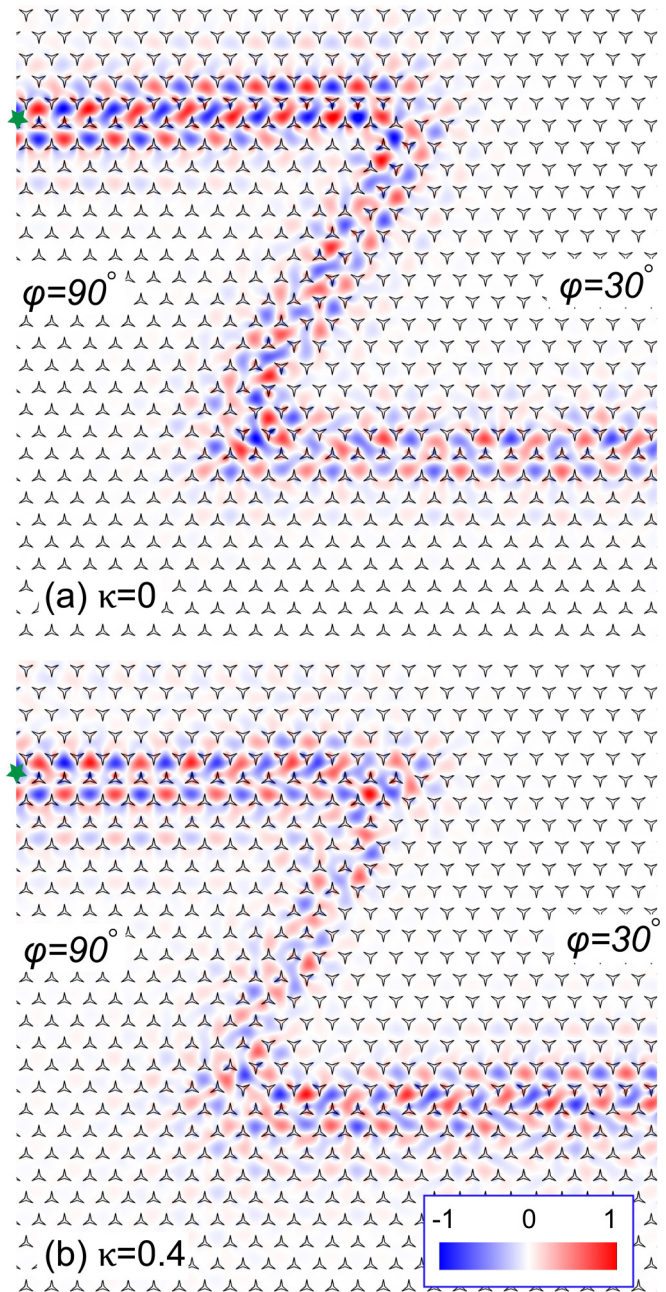

FIG. 11. Numerical simulation of wave propagation in a valley interfacial state along a Z-shape bend between two valley-contrasting photonic crystals of $\varphi = 30°$ and $\varphi = 90°$. (a) $\kappa = 0.0$ and (b) $\kappa = 0.4$. The green star denotes the point source operating at (a) $\omega = 0.9$ and (b) $0.91\, 2\pi c/a$. The values on the color bar denote the $\mathrm{Re}(E_z)$ in units of V/m.

indicate that the QVH photonic crystal waveguides presented here are not the ordinary photonic crystal waveguides and could have promising applications for, e.g., designing photonic valleytronic devices [19].

IV. CONCLUSIONS

In conclusion, we have carried a comprehensive theoretical study on the topological phases in 2D photonic crystals without $\mathcal{T}$ and $\mathcal{P}$ symmetries. As an example, we consider a hexagonal

lattice consisting of triangular gyromagnetic rods. Here the gyromagnetic material breaks $\mathcal{T}$ invariance while the triangular rods break $\mathcal{P}$ symmetry. Remarkably, we discover that the photonic crystal houses QAH phases with different gap Chern numbers (C_g) including $|C_g| = 2$ as well as QVH phases with contrasting valley Chern numbers (C_v). Moreover, phase transitions among these topological phases, such as from QAH to QVH and vice versa, can be realized by a simple rotation of the orientation of the rods. Our band theoretical analyses reveal that the Dirac nodes at the K and K' valleys in the momentum space are produced and protected by the mirror symmetry (m_y) instead of the $\mathcal{P}$ symmetry in the $\mathcal{P}$-invariant crystals, and they become gapped when either $\mathcal{T}$ or m_y symmetry is broken, leading to a QAH or QVH phase, respectively. Furthermore, the high Chern number ($C_g = -2$) QAH phase arises when the rare triply degenerate nodal points [28,37] rather than pairs of Dirac nodes [10] are gapped by breaking $\mathcal{T}$ symmetry. Therefore, our proposed photonic crystal would provide a platform for exploring transitions among intriguing topological phases which may be very difficult to realize in electronic systems.

Our electromagnetic simulations of wave propagation either along the edges of our crystal capped with a metal wall or in the interfaces between two variants of our crystal with different rod orientations, demonstrate reflection-immune one-way light transports in both straight interfaces and Z-shape bends. Furthermore, we find that the second topologically nontrivial gap is not only large but also independent of the orientation of the triangular rods, and thus the topologically protected one-way wave propagation would be very robust against disorders such as misalignments of the triangular rods in the photonic crystal introduced during the fabrication processes. Therefore, our proposed crystal would also have promising potentials for device applications in photonics such as reflection-free waveguides and topological one-way circuits.

[1] M. Z. Hasan and C. L. Kane, Colloquium: Topological insulators, Rev. Mod. Phys. **82**, 3045 (2010).

[2] L. Lu, J. D. Joannopoulos, and M. Soljačić, Topological photonics, Nat. Photon. **8**, 821 (2014).

[3] F. D. M. Haldane, Model for a Quantum Hall Effect Without Landau Levels: Condensed-Matter Realization of the "Parity Anomaly", Phys. Rev. Lett. **61**, 2015 (1988).

[4] H. M. Weng, R. Yu, X. Hu, X. Dai, and Z. Fang, Quantum anomalous Hall effect and related topological electronic states, Adv. Phys. **64**, 227 (2015).

[5] C.-Z. Chang, J. Zhang, X. Feng, J. Shen, Z. Zhang, M. Guo, K. Li, Y. Qu, P. Wei, L.-L. Wang, Z.-Q. Ji, Y. Feng, S. Ji, X. Chen, J. Jia, X. Dai, Z. Fang, S.-C. Zhang, K. He, Y. Wang, L. Lu, X.-C. Ma, and Q.-K. Xue, Experimental observation of the quantum anomalous Hall effect in a magnetic topological insulator, Science **340**, 167 (2013).

[6] F. D. M. Haldane and S. Raghu, Possible Realization of Directional Optical Waveguides in Photonic Crystals with Broken Time-Reversal Symmetry, Phys. Rev. Lett. **100**, 013904 (2008).

[7] S. Raghu and F. D. M. Haldane, Analogs of quantum-Hall-effect edge states in photonic crystals, Phys. Rev. A **78**, 033834 (2008).

[8] Z. Wang, Y. D. Chong, J. D. Joannopoulos, and M. Soljačić, Reflection-Free One-Way Edge Modes in a Gyromagnetic Photonic Crystal, Phys. Rev. Lett. **100**, 013905 (2008).

[9] Z. Wang, Y. Chong, J. D. Joannopoulos, and M. Soljačić, Observation of unidirectional backscattering-immune topological electromagnetic states, Nature (London) **461**, 772 (2009).

[10] S. A. Skirlo, L. Lu, and M. Soljačić, Multimode One-Way Waveguides of Large Chern Numbers, Phys. Rev. Lett. **113**, 113904 (2014).

[11] C. He, X.-L. Chen, M.-H. Lu, X.-F. Li, W.-W. Wan, X.-S. Qian, R.-C. Yin, and Y.-F. Chen, Tunable one-way cross-waveguide splitter based on gyromagnetic photonic crystal, Appl. Phys. Lett. **96**, 111111 (2010).

[12] Z. Wang, L. Shen, Z. Yu, X. Zhang, and X. Zheng, Highly efficient photonic-crystal splitters based on one-way waveguiding, J. Opt. Soc. Am. B **30**, 173 (2013).

[13] S. A. Skirlo, L. Lu, Y. Igarashi, Q. Yan, J. Joannopoulos, and M. Soljačić, Experimental Observation of Large Chern Numbers in Photonic Crystals, Phys. Rev. Lett. **115**, 253901 (2015).

[14] T. Ochiai and M. Onoda, Photonic analog of graphene model and its extension: Dirac cone, symmetry, and edge states, Phys. Rev. B **80**, 155103 (2009).

[15] W.-Y. He and C. T. Chan, The emergence of Dirac points in photonic crystals with mirror symmetry, Sci. Rep. **5**, 8186 (2015).

[16] D. Xiao, M.-C. Chang, and Q. Niu, Berry phase effects on electronic properties, Rev. Mod. Phys. **82**, 1959 (2010).

[17] D. Xiao, W. Yao, and Q. Niu, Valley-Contrasting Physics in Graphene Magnetic Moment and Topological Transport, Phys. Rev. Lett. **99**, 236809 (2007).

[18] K. F. Mak, K. L. McGill, J. Park, and P. L. McEuen, The valley Hall effect in MoS₂ transistors, Science **344**, 1489 (2014).

[19] T. Ma and G. Shvets, All-Si valley-Hall photonic topological insulator, New J. Phys. **18**, 025012 (2016).

[20] X.-D. Chen, F.-L. Zhao, M. Chen, and J.-W. Dong, Valley-contrasting physics in all-dielectric photonic crystals: Orbital angular momentum and topological propagation, Phys. Rev. B **96**, 020202 (2017).

[21] J.-W. Dong, X.-D. Chen, H. Zhu, Y. Wang, and X. Zhang, Valley photonic crystals for control of spin and topology, Nat. Mater. **16**, 298 (2017).

[22] D. M. Pozar, *Microwave Engineering*, 2nd ed. (Wiley, New York, 1997).

[23] https://www.comsol.com

[24] T. Fukui, Y. Hatsugai, and H. Suzuki, Chern numbers in discretized Brillouin zone: Efficient method of computing (spin) Hall conductances, J. Phys. Soc. Jpn. **74**, 1674 (2005).

[25] Y. Hatsugai, Chern Number and Edge States in the Integer Quantum Hall Effect, Phys. Rev. Lett. **71**, 3697 (1993).

[26] J. D. Joannopoulos, S. G. Johnson, J. N. Winn, and R. D. Meade, *Photonic Crystals: Molding the Flow of Light*, 2nd ed. (Princeton University Press, Princeton, NJ, 2008).

[27] X. Huang, Y. Lai, Z. H. Hang, H. Zheng, and C. T. Chan, Dirac cones induced by accidental degeneracy in photonic crystals and zero-refractive-index materials, Nat. Mater. **10**, 582 (2011).

[28] P. Wang, L. Lu, and K. Bertoldi, Topological Phononic Crystals with One-Way Elastic Edge Waves, Phys. Rev. Lett. **115**, 104302 (2015).

[29] H. Weng, C. Fang, Z. Fang, and X. Dai, Topological semimetals with triply degenerate nodal points in θ-phase tantalum nitride, Phys. Rev. B **93**, 241202 (2016).

[30] Z. Zhu, G. W. Winkler, Q. S. Wu, J. Li, and A. A. Soluyanov, Triple Point Topological Metals, Phys. Rev. X **6**, 031003 (2016).

[31] B. Q. Lv, Z.-L. Feng, Q.-N. Xu, X. Gao, J.-Z. Ma, L.-Y. Kong, P. Richard, Y.-B. Huang, V. N. Strocov, C. Fang, H.-M. Weng, Y.-G. Shi, T. Qian, and H. Ding, Observation of three-component fermions in the topological semimetal molybdenum phosphide, Nature (London) **546**, 627 (2017).

[32] G. Y. Guo, S. Murakami, T.-W. Chen, and N. Nagaosa, Intrinsic Spin Hall Effect in Platinum: First-Principles Calculations, Phys. Rev. Lett. **100**, 096401 (2008).

[33] W. Feng, Y. Yao, W. Zhu, J. Zhou, W. Yao, and D. Xiao, Intrinsic spin Hall effect in monolayers of group-VI dichalcogenides: A first-principles study, Phys. Rev. B **86**, 165108 (2012).

[34] T.-W. Chen, Z.-R. Xiao, D.-W. Chiou, and G.-Y. Guo, High Chern number quantum anomalous Hall phases in graphene with Haldane orbital coupling, Phys. Rev. B **84**, 165453 (2011).

[35] H.-C. Hsu, M.-J. Jhang, T.-W. Chen, and G.-Y. Guo, Topological phase transitions in an inverted InAs/GaSb quantum well driven by titled magnetic fields, Phys. Rev. B **95**, 195408 (2017).

[36] A. B. Khanikaev, S. H. Mousavi, W.-K. Tse, M. Kargarian, A. H. MacDonald, and G. Shvets, Photonic topological insulators, Nat. Mater. **12**, 233 (2013).

[37] J. Mei, Y. Wu, C. T. Chan, and Z.-Q. Zhang, First-principles study of Dirac and Dirac-like cones in phononic and photonic crystals, Phys. Rev. B **86**, 035141 (2012).